Computer Modeling in
Engineering & Sciences

Tech Science Press

DOI: 10.32604/cmes.2022.018665

ARTICLE

Theoretical Investigation of Two-Dimensional Nonlinear Radiative Thermionics in Nano-MHD for Solar Insolation: A Semi-Empirical Approach

Usman Inayat[1,*], **Shaukat Iqbal**[1] **and Tareq Manzoor**[2]

[1]School of Systems and Technology, University of Management and Technology, Lahore, 54000, Pakistan

[2]Energy Research Centre, COMSATS University Islamabad, Lahore Campus, Lahore, 54000, Pakistan

[*]Corresponding Author: Usman Inayat. Email: usman.inayat@umt.edu.pk

Received: 09 August 2021 Accepted: 02 September 2021

ABSTRACT

In this contemporary study, theoritical investigation of nanofluidic model is thought-out. Two-dimensional nanomaterials based mixed flow is considered here. Convective solar radiative heat transport properties have been investigated over a nonlinearly stretched wall in the presence of magneto-hydrodynamic (MHD), by innovative application of semi analytical "optimal homotopy asymptotic method (OHAM)". OHAM does not require any discretization, linearization and small parameter assumption. OHAM describes extremely precise $1^{st}/2^{nd}$ order solutions without the need of computing further higher order terms, therefore, fast convergence is observed. Nanofluidic governing model is transformed into system of ordinary differential equations (ODEs) by exploitation of similarity transformation. To study the significance of radiation parameter along with thermophoresis parameter, a semi analytical solver is applied to the transformed system. In this work, Brownian motion , influence of magnetic field, Lewis number, Prandtl number, Eckert number and Biot number have investigated on velocity, temperature and nanoparticle concentration profiles. The study provides sufficient number of graphical representations to demonstrate the inspiration of mentioned parameters.

KEYWORDS

Magneto-hydrodynamic (MHD); OHAM; nanofluid; solar radiative; stretched wall

1 Introduction

The most abundance renewable energy source for best alternative to conventional fossil fuel-based generation is solar energy. Electric energy and heat energy can be generated through sun light using photoelectric effect on photovoltaic panels and photothermal conversion on concentrated solar thermal plants, respectively. The increasing rate of solar absorption helps in improving energy output production of both photovoltaic panels and concentrated solar thermal plants. The efficient absorption of solar energy results in reliable use of renewable energy and better conversion into thermal energy, which results in least dependence on fossil fuels. However, the current heat collectors and photovoltaic panels suffer from inefficient sunlight absorption that results in signification energy loss and low efficiency. In this regard, water dispersed nanoparticles are being extensively studied for improving sunlight absorption. Various nanomaterials have been proposed and tested for ameliorating sunlight absorption efficiency. The sunlight absorption capability is improved by using photoactive nanomaterials for polymeric photovoltaic panels. It is known that these polymeric photovoltaic panels absorb photons with bandgap of 2-ev. Therefore, nanomaterials are needed to widen this energy bandgap for absorbing more sunlight. In this regard, a hybrid solar cell was proposed for more solar energy absorption from visible to near-infrared energy band.

The heterojunction photovoltaic cells were examined for analyzing their solar absorption enhancement capability using half-coaxial crystalline silicon nanowire arrays [1]. High bandgap solar cell was integrated with upconverter at its for stronger sunlight absorption in the near infrared region [2]. The broadband absorption enhancement was achieved in Si films by their crystallization in liquid phase on textured glass. The absorption enhancement was increased by 36.3% as compared to planar reference film [3]. A two-dimensional photonic-structured perovskite photovoltaic cell was investigated, which provided 65.7% more absorption efficiency over the visible range [4]. Photonic crystals were placed on the top surface of microcrystalline silicon solar cells to enhance light absorption with the exploitation of resonant effects in photonic crystal. The efficiency was reported to be increased by 11% due to enhanced short circuit current density [5]. The dye-sensitized photovoltaic cells were combined with uncapped lead sulfide nanocrystals to achieve increase in absorption capability by 7.9% [6].

The index-guiding microstructured optical fiber, which is ionic-liquid adorned, were adopted to construct an optical fiber light detector by splicing it with two air holes in innermost layer. It was reported to have power density sensitivity to achieve value of $1.529\,\mathrm{dB/(mW.mm^2)}$ [7]. The titanium nitride nanoparticles were investigated in water with experimental results to report higher sunlight absorption efficiency as compared to carbon nanoparticles [8]. The surface mounted gold particles based copper-doped TiO_2 nanocomposites were synthesized using a facile step method. It was observed that they were able to enhance more visible light spectrum absorption as compared to pure TiO_2 and copper-doped TiO_2 [9]. The light energy concertation was achieved at mesoscale volumes using light-absorbing nanoparticles contained aqueous solutions. The high efficiency steam was obtained using sunlight even in case of having far below boiling temperature of the bulk fluid [10]. The experimental results were presented to show that the rapid water vaporization with sunlight can be achieved using silicon nanoparticles in water [11]. Rapid sunlight to heat conversion was achieved using plasmonic nanocomposites with filler concentration at volumetric ppm level [12]. Collocation and optimal homotopy asymptotic methods had been used for investigation of third grade non-Newtonian blood fluid [13]. Similarly, third grade non-Newtonian blood flow had also been investigated by solving their partial differential equations using differential quadrature method [14]. The performance of optimal homotopy asymptotic method (OHAM) found better as compared to fourth order Runge–Kutta numerical method, while investigating micropolar fluid [15]. OHAM had also been used for computational analysis of micropolar fluid flow [16]. The heat transfer analysis of solar collectors had been performed using OHAM and homotopy perturbation method [17]. Peristaltic nanofluid flow had been analyzed using differential tranformation method to study the impacts of Brownian and thermophoresis motions on its flow for drug delivery applications [18]. The fourth order Runge–Kutta numerical method with shooting technique had been adopted for solving the governing equations of nanofluid towards a stretching sheet [19]. The solar energy induced stagnation-point fluid flow was investigated using Rooseland approximation and shooting technique–based fourth–fifth order

Runge–Kutta method. It was reported that the liquid absorbed higher solar radiations due to excessive mobility of nanoparticles [20]. The numerical study magneto–hydrodynamic (MHD) nanofluid flow was performed to analyze the effect of solar energy on fluid flow using Keller–Box numerical approach [21]. The summary of existing solution methods and fluid types for different applications has been presented in Table 1. Besides these, the dynamics of nanofluidic problems have also been discussed in the literature for different application fields.

Table 1: Overview of existing solution methods and fluid types for different applications

Reference	Fluid application	Solution methods
[13]	Third grade non-Newtonian blood	Collocation and optimal homotopy asymptotic methods
[14]	Pulsatile blood flow in femoral and coronary arteries	Differential quadrature method
[15]	Two dimensional micropolar fluid between two porous disks	Optimal homotopy asymptotic method
[16]	Micropolar fluid between porous and non-porous disk	Optimal homotopy asymptotic method
[17]	Air-heating flat-plate solar collectors	Optimal homotopy asymptotic and homotopy perturbation methods
[18]	Peristaltic nanofluid for drug delivery	Differential transformation method
[19]	Nanofluid towards a stretching sheet	fourth order Runge–Kutta numerical method
[20]	Solar energy induced stagnation-point fluid flow	fourth–fifth order Runge–Kutta method
[21]	Solar energy incuded magneto–hydrodynamic nanofluid flow	Keller–Box numerical method

This conducted research explored nanofludics systems numerically and graphically. The less research has been performed on the application of the two-dimensional non-linear radiative heat transfer in the nanofluid flow. The major contributions of the proposed work are:

- Optimal homotopy asymptotic method has been proposed for the numerical solutions of two-dimensional non-linear radiative heat transfer in the nanofluid.
- The performance of OHAM method has been analyzed in terms of convergence rate and the results prove its faster convergence.
- The dynamics of the nanofluid have also been analyzed in respect of Velocity, Nanoparticle concentration profiles, and Temperature profiles studied with the effect of Magnetic parameter, Radiation parameter, Lewis number, Eckert number, Biot number, Prandtl number, Thermophoresis parameter, and Brownian motion.

Rest of the paper is organized as follows: Section 2 presents modeling of nanofluid flow over a stretched sheet, Section 3 discusses optimal homotopy asymptotic method for the numerical solutions, Section 4 provides solution and results to show effectiveness of the proposed method, and Section 5 concludes the proposed research.

2 Modeling of Two-Dimensional Nonlinear Radiative Thermionics in Nano-MHD

Suppose the flow of nanofluid over stretched sheet shown in Fig. 1, with convective heating at y = 0. Along x-direction the stretching velocity is $\mu_\omega = \alpha x$. B_0 is the magnetic field perpendicular to the flow. $\mu_\infty(x) = \beta x$ is the free stream velocity. The analysis of heat transfer is done under the influence of viscous dissipation, Joule heating and thermal radiations, with the combined effect of thermophoresis and Brownian motion.

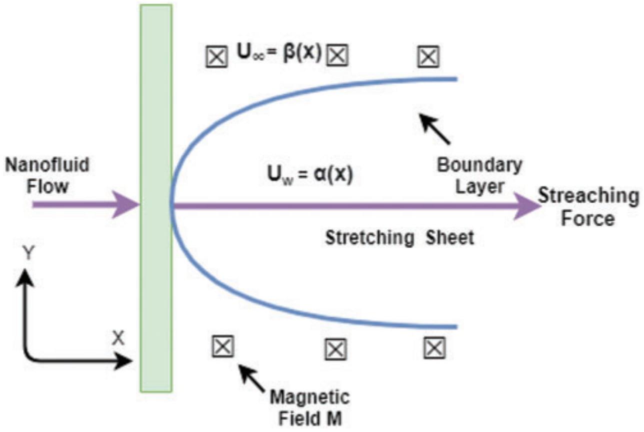

Figure 1: Coordinate system for the physical stretched sheet model

The governing equations of the heat flow under typical boundry conditions can be expressed as [22,23]:

$$\frac{\partial \mu}{\partial x} + \frac{\partial \upsilon}{\partial y} = 0 \tag{1}$$

$$\mu \frac{\partial \mu}{\partial x} + \upsilon \frac{\partial \upsilon}{\partial y} = \mu_\infty \frac{d\mu_\infty}{\partial x} + \upsilon_f \frac{\partial^2 \mu}{\partial y^2} - \frac{\sigma_e {B_0}^2}{\chi_f}(\mu - \mu_\infty), \tag{2}$$

$$\begin{aligned} \mu \frac{\partial T}{\partial x} + \upsilon \frac{\partial T}{\partial y} = \zeta \frac{\partial^2 T}{\partial y^2} + \frac{\upsilon_f}{C_f}\left(\frac{\partial \mu}{\partial y}\right)^2 - \frac{1}{(\chi C)_f}\frac{\partial m_r}{\partial z} + \frac{\sigma_e {B_0}^2}{(\chi C)_f}(\mu_\infty - \mu) \\ + \Upsilon K_B \left(\left(\frac{\partial T}{\partial y}\frac{\partial C}{\partial y}\right) + \frac{K_T}{T_\infty}\left(\frac{\partial T}{\partial y}\right)^2\right), \end{aligned} \tag{3}$$

$$\mu \frac{\partial C}{\partial x} + \upsilon \frac{\partial C}{\partial y} = K_B\left(\frac{\partial^2 C}{\partial y^2}\right) + \frac{K_T}{T_\infty}\left(\frac{\partial^2 T}{\partial y^2}\right). \tag{4}$$

In above Eqs. (1)–(4) velocity component along x-axis is μ and along y-axis is υ. K_B is the Brownian parameter, K_T is the thermophoretic diffusion parameter. ζ is the base fluid thermal diffusivity, χ_f is the density of base fluid, heat capacities are denoted by $(\chi C)_f$ and $(\chi C)_p$,

m_r represents parameter of radioactive heat flux and nanoparticale concentration is represented by C, where,

$$m_r = -\frac{4\sum}{3n^*}\frac{\partial T^4}{\partial y} \tag{5}$$

In Eq. (5), σ denotes the Stefan-Boltzman constant, n^* represents the mean absorption coefficient. Eqs. (2)–(4) can be transformed to:

$$\frac{d^3g}{d\eta^3} + g\frac{d^2g}{d\eta^2} - \left(\frac{dg}{d\eta}\right)^2 + M\left(\gamma - \frac{dg}{d\eta}\right) = 0, \tag{6}$$

$$\begin{aligned}&\left(K_R(\phi^3(\phi_\omega - 1) + 1)\frac{d\phi}{d\eta} + 1\right) + P_R M E_c\left(\gamma - \frac{dg}{d\eta}\right)^2 + gP_R\frac{d\phi}{d\eta}\\ &\quad + P_R E_c\left(\frac{d^2g}{d\eta^2}\right) + P_R N_B\frac{d\phi}{d\eta}\frac{d\theta}{d\eta} + P_R N_T\left(\frac{d^2g}{d\eta^2}\right) = 0,\end{aligned} \tag{7}$$

$$\frac{d^2\theta}{d\eta^2} + gL_E\frac{d\theta}{d\eta} + \frac{N_T}{N_B}\frac{d^2\phi}{d\eta^2} = 0 \tag{8}$$

The boundary conditions will be of the form:

$$\begin{aligned}&g'(0) = 0, \quad g'(\infty) \to \gamma, \quad g'(0) = 1,\\ &\qquad \theta(0) = 1, \quad \theta(\infty) \to 0,\\ &\phi'(0) = -\lambda[1 - \phi(0)], \quad \phi(\infty) \to 0.\end{aligned}$$

OHAM is used to solve Eqs. (6)–(8) under given boundary conditions.

3 Numerical Method

3.1 Formulation of OHAM

The idea of optimal homotopy asymptotic method (OHAM) is discussed in [24–29]. Governing differential equation is written as:

$$B(u(\kappa)) + w(\kappa) = 0, \quad \kappa \in \Omega \tag{9}$$

$$A(u) = 0 \tag{10}$$

$B(u) = L(u) + S(u)$ where L is a linear component and S is the nonlinear component. It is worth noting that we have a great freedom to choose the L part from the model, therefore it does not need to get the first solution (initial guess). κ is independent variable, Ω is domain, $u(\kappa)$ is unknown function, $w(\kappa)$ is a known function. Substituting $B(u)$ in (9),

$$L(u(\kappa)) + w(\kappa) + S(u(\kappa)) = 0, \tag{11}$$

by applying OHAM on (11):

$$(1-q)[L(\Phi(\kappa,q)) + w(\kappa) = H(q)[L(\Phi(\kappa,q)) + w(\kappa) + S(\Phi(\kappa,q))]', \tag{12}$$

$$A(\Phi(\kappa,q)) = 0$$

where $q \in [0, 1]$ is an embedding parameter, nonzero auxiliary function $H(q)$ at $q \neq 0$ with $H(0) = 0$, $\Phi(\kappa, q)$ is an unknown function. For $q = 0, 1$

$$\Phi(\kappa, 0) = u_0(\kappa), \quad \Phi(\kappa, 1) = u(\kappa) \tag{13}$$

With the change in value of P from 0 to 1, $\Phi(\kappa, q)$ varies from $u_0(\kappa)$ to $u(\kappa)$. Putting $q = 0$ in (12):

$$L(u_0(\kappa)) + w(\kappa) = 0, \quad A(u_0) = 0 \tag{14}$$

Auxiliary function will be of the form:

$$H(q) = qC_1 + q^2C_2 + q^3C_3 + \cdots, \tag{15}$$

where C_1, C_2, C_3,... are con stants to be evaluated. By applying Taylor's series with respect to q for expansion we get:

$$\Phi(\kappa, q, C_i) = u_0(\kappa) + \sum_{n=1}^{\infty} u_n(\kappa; C_i)q^n, \quad i = 1, 2, 3, \ldots.. \tag{16}$$

Comparing (16) and (12), we get following coefficients

$$L(u_1(\kappa)) = C_1S_0(u_0(\kappa)), \quad A(u_1) = 0, \tag{17}$$

$$L(u_2(\kappa)) - L(u_1(\kappa)) = C_2S_0(u_0(\kappa)) + C_1[L(u_1(\kappa)) + S_1(u_0(\kappa), u_1(\kappa))] \tag{18}$$

$$A(u_2) = 0 \tag{19}$$

where $S_{n-i}(u_0(\kappa), u_1(\kappa), \ldots, u_{n-i}(\kappa))$ is the coefficient of q^{n-i}. expansion of $S(\Phi(\kappa;q))$ gives that

$$S(\Phi(\kappa; q, C_i)) = S_0(u_0(\kappa)) + \sum_{n\geq 1} s_n(u_0, u_1, \ldots, u_n)q^n. \tag{20}$$

Convergence of the Eq. (16) depends on the values of auxiliary constants $C_1, C_2, C_3, C_4 \ldots$ For $q = 1$

$$u'(\kappa; C_i) = u_0(\kappa) + \sum_{n\geq 1} u_n(\kappa; C_i) \tag{21}$$

From (21) and (11), we get the residual expansion

$$R(\kappa; C_i) = L(\acute{u}(\kappa; C_i)) + w(\kappa) + S(\acute{u}(\kappa; C_i)) \tag{22}$$

We will get exact solution of $\acute{u}(\kappa; C_i)$ if $R(\kappa; C_i) = 0$, it is not always true for nonlinear systems. For the determinations of auxiliary constants $C_1, C_2, C_3, \ldots$, following methods can be used:

- Galerkin's Method,
- Ritz Method,
- Least Squares Method and
- Collocation Method

To find the optimal values of auxiliary constants. Method of least square is the most common method to optimize the errors by taking the square of the residuals over the given domain to get the following functional:

$$J(C_i) = \int_{x_1}^{x_2} R^2(\kappa, C_1, C_2, C_3, \ldots) d\kappa, \tag{23}$$

where x_1 and x_2 are the values depending on the given system. The optimal values of C_1, C_2, C_3,... can be evaluated with minimum error from:

$$\frac{\partial J}{\partial C_1} = \frac{\partial J}{\partial C_2} = \frac{\partial J}{\partial C_3} = \ldots = \frac{\partial J}{\partial C_n} = 0. \tag{24}$$

Solving the above system of algebraic equations obtained in Eq. (24), we get the values of C_1, C_2, C_3,.... Replacing the values of C_1, C_2, C_3,...C_i in Eq. (10), we get the approximate solution. Fig. 2 explains the process of modeling and solution of MHD problem using OHAM.

3.2 Validation of OHAM

Validation of the OHAM technique is an essential part of a theoretical study. The aim of validation is to ensure the computations are reliable. For this purpose, we considered singular initial value Lane-Emden [30] model to evaluate our semi-empirical technique. Indeed, OHAM is known for its easy implementation, effectiveness for solving singular phenomena, and producing efficient results with minimum computations. The general representation of Lane-Emden equation is given as follows:

$$v'' + \frac{n}{x} v' + f(v) = g(x), \quad 0 < x < 1, n \geq 1. \tag{25}$$

with initial conditions

$$v(0) = \gamma, \quad v'(0) = \delta.$$

where $f(v)$ is a real valued continuous function, γ, δ and n are constants. The most common form of $f(v) = v^{\lambda}$, here λ is tropic index. From literature it observed that the solutions of the Lane-Emden equation could be given in closed form if tropic index is $0 \leq \lambda \leq 5$. For $\lambda = 3$, $n = 2$ and $g(x) = x^5 + 30$, Eq. (25) will become:

$$\frac{d^2 v(x)}{dx^2} = -\frac{2}{x}\left(\frac{d(v(x))}{dx}\right) - v + x^5 + 30, \quad 0 < x \leq 1, \tag{26}$$

with boundary conditions $v(0) = 0$ and $v'(0) = 0$. The exact solution of the Eq. (26) is $v(x) = x^5$ [31].

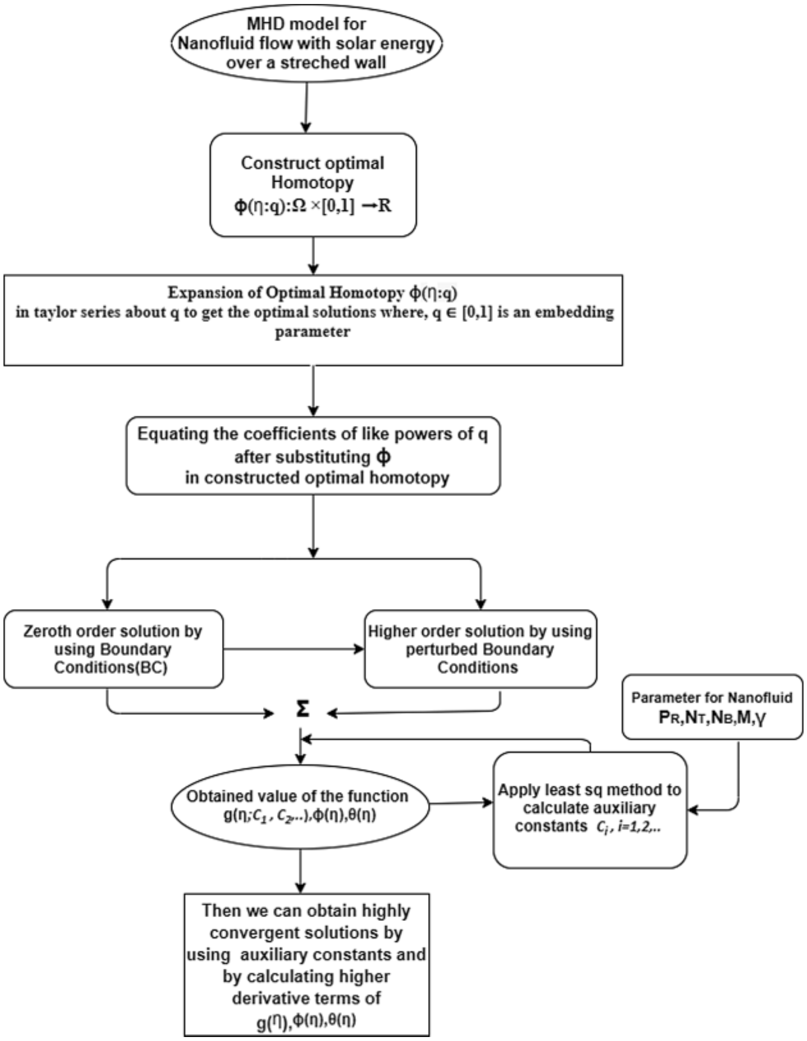

Figure 2: Schematic representation for the MHD flow analysis of nanofluid over a non-linear stretching sheet

For $\lambda = 1$, $n = 2$ and $g(x) = x^6 + 6$, Eq. (25) will become:

$$\frac{d^2v(x)}{dx^2} = -\frac{2}{x}\left(\frac{d(v(x))}{dx}\right) - v^3 + x^6 + 6, \quad 0 < x \leq 1, \tag{27}$$

having boundary conditions $v(0) = 0$ and $v'(0) = 0$. The exact solution of the Eq. (27) is $v(x) = x^2$ [31].

By applying OHAM scheme Eqs. (12)–(24) subject to the given boundary conditions to evaluate solutions denoted by v_{OHAM}. As shown in Table 2, the effectiveness of OHAM is validated using absolute errors $|v_{Exact} - v_{OHAM}|$, for Eqs. (26) and (27). Table 2 verifies that accuracy is achieved even with the second order approximations.

Table 2: Validation of OHAM using absolute errors comparison for Lane-Emden model

x	Model 1 (Eq. (26))			Model 2 (Eq. (27))		
	v_{Exact}	v_{OHAM}	$\lvert v_{Exact} - v_{OHAM}\rvert$	v_{Exact}	v_{OHAM}	$\lvert v_{Exact} - v_{OHAM}\rvert$
	0	0	0	0	0	0
0.1	0.00001	0.00001	1.9129×10^{-13}	0.01	0.01	5.08092×10^{-14}
0.2	0.00032	0.00032	2.32418×10^{-11}	0.04	0.04	1.30061×10^{-11}
0.3	0.00243	0.00243	3.62995×10^{-10}	0.09	0.09	3.3304×10^{-10}
0.4	0.01024	0.01024	2.38195×10^{-9}	0.16	0.16	3.31194×10^{-9}
0.5	0.03125	0.03125	9.45552×10^{-9}	0.25	0.25	1.94424×10^{-8}
0.6	0.07776	0.07776	2.6459×10^{-8}	0.36	0.36	8.02049×10^{-8}
0.7	0.16807	0.16807	5.5833×10^{-8}	0.49	0.49	2.49742×10^{-7}
0.8	0.32768	0.32768	9.05342×10^{-8}	0.64	0.640001	5.89492×10^{-7}
0.9	0.59049	0.59049	1.11444×10^{-7}	0.81	0.810001	9.84671×10^{-7}
1.0	1	1.0000001	1.12014×10^{-7}	1	1.000001	1.09369×10^{-6}

4 Solutions and Results

In this section, OHAM is applied to nonlinear ODE's Eqs. (6)–(8). The homotopy of Eq. (6) is constructed as:

$$(1-q)(g'''(\eta)) - (qC_1 + q^2C_2 + q^3C_3)(g'''(\eta) + gg''(\eta) - g'(\eta)^2 + M(\gamma - g'(\eta)) = 0, \tag{28}$$

We consider $g(\eta)$ as follows:

$$g(\eta) = g_0(\eta) + qg_1(\eta) + q^2g_2(\eta) \tag{29}$$

By solving Eqs. (28) and (29), after simplification and equating like powers of q-terms, we get

$$q^0 : g_0'''(\eta) = 0, \tag{30}$$

$$q^1 : -\gamma MC_1 + MC_1g_0'(\eta) + C_1g_0'(\eta)^2 - g_0(\eta)C_1g_0''(\eta) - g_0'''(\eta) - C_1g_0'''(\eta) - g_1'''(\eta) = 0, \tag{31}$$

$$q^2 : -\gamma MC_2 + MC_2g_0'(\eta) + C_2g_0'(\eta)^2 + MC_1g_1'(\eta) + 2C_1g_0'(\eta)g_1'(\eta) - g_1(\eta)C_1g_0''(\eta) - g_0(\eta)C_2g_0''(\eta)$$

$$-g_0(\eta)C_1g_1''(\eta) - C_2g_0'''(\eta) - C_1g_1'''(\eta) - g_1'''(\eta) + g_2'''(\eta) = 0. \tag{32}$$

The homotopy of Eq. (7) is constructed as:

$$(1-q)(K_R\phi''(\eta)) - (qC_1 + q^2C_2 + q^3C_3)(B + P_R(g\phi'(\eta) + N_B\phi'(\eta)\theta(\eta) + N_T\phi'(\eta)^2 + E_Cg''(\eta)^2 + ME_C(\gamma - g'(\eta))^2)) = 0. \tag{33}$$

We consider $\phi(\eta)$ as follows:

$$\phi(\eta) = \phi_0(\eta) + q\phi_1(\eta) = 0 \tag{34}$$

By solving Eqs. (33) and (34), after simplification and equating like powers of q-terms, we get

$$q^0 : K_R\phi_0''(\eta) = 0, \tag{35}$$

$$
\begin{aligned}
q^1 :& -P_R E_C \gamma^2 M C_1 + 2P_R E_C \gamma M C_1 g_{0'}(\eta) - 2P_R E_C \gamma M C_1 g_{0'}(\eta)^2 \\
& -P_R g_0(\eta) C_1 \phi_{0'}(\eta) - N_T P_R C_1 \phi_{0'}(\eta)^2 \\
& -3K_R \phi\omega C_1 \phi_0(\eta^2)\phi_0'(\eta)^2 - N_B P_R C_1 \phi_0'(\eta)\theta_0'(\eta) - P_R E_C C_1 g_0{}''(\eta)^2 - K_R \phi_0^{''}(\eta) - K_R C_1 \phi_0^{''}(\eta), \\
& +3K_R C_1 \phi_0(\eta)^2 \phi_0(\eta)^2 + K_R C_1 \phi_0(\eta)^3 \phi_0''(\eta) - K_R \phi\omega C_1 \phi_0(xi)^3 \phi_0''(\eta) + K_R \phi_1''(\eta) = 0. \qquad (36)
\end{aligned}
$$

The homotopy of Eq. (8) is constructed as:

$$
(1-q)(\theta''(\eta) - (qC_1 + q^2 C_2 + q^3 C_3)\left(\theta''(\eta) + L_E g\theta'(\eta) + \frac{N_T}{N_B}\phi''(\eta)\right) = 0. \qquad (37)
$$

We consider $\theta(\eta)$ as follows:

$$
\theta(\eta) = \theta_0(\eta) + q\theta_1(\eta) + q^2\theta_2(\eta) \qquad (38)
$$

By solving Eqs. (37) and (38), after simplification and equating like powers of q-terms, we get

$$
q^0 : \theta_0''(\eta) = 0, \qquad (39)
$$

$$
q^1 : -L_E g_0(\eta) C_1 \theta_0'(\eta) - \frac{N_T C_1 \phi_0''(\eta)}{N_B} - \theta_0''(\eta) - C_1 \theta_0''(\eta) + \theta_1''(\eta) = 0, \qquad (40)
$$

$$
\begin{aligned}
q^2 :& -L_E g_1(\eta) C_1 \theta_0'(\eta) - L_E g_0(\eta) C_2 \theta_0' - L_E g_0(\eta) C_1 \theta_1' - \frac{N_T C_2 \phi_0''(\eta)}{N_B} - \frac{N_T C_1 \phi_1''(\eta)}{N_B} - C_2 \theta_0''(\eta) \\
& -\theta_1''(\eta) - C_1 \theta_1''(\eta) + \theta_2''(\eta) = 0. \qquad (41)
\end{aligned}
$$

The modified equations obtained from OHAM have been solved using boundary conditions which are provided in Section 2. For solar application analysis of OHAM, solar radiation's impact in a magnetic field conducted over an extended plate with a nanofluid limit layer has been investigated to illustrate the impact of radiation parameter Velocity profile $g(\eta)$ with the magnetic parameter M and γ which is ratio between $\mu_\infty(x)$ and $\mu_w(x)$. Influence on local Nusselt number $\phi'(\eta)$ and temperature profile $\phi(\eta)$ are also analyzed by varying Eckert Number E_c, magnetic field parameter M, radiation parameter K_r, Brownian motion parameter N_B, Biot number λ, Prandtl number P_R, thermophoresis parameter N_T, and Lewis number L_E. Quantitative illustration of the results for local Nusselt number and local Sherwood number for different physical quantities is provided, in Table 3. The Sherwood number $\theta'(\eta)$ and nanoparticle concentration Profile $\theta(\eta)$ are also analyzed graphically as presented below.

Velocity profile has been presented in Fig. 3 in accordance with diverse values of the magnetic parameter M with γ which is ratio between $\mu_\infty(x)$ and $\mu_w(x)$. The magnetic parameter M causes the velocity profile to decrease. Fig. 4 illustrates the diverse values of γ with fixed value of the magnetic parameter on velocity profile. It is observed with the increase in value of γ, $g'(\eta)$ increases.

Table 3: Local Nusslet and local Sherwood numbers for $\lambda = 0.5$, $\gamma = 0.5$, $P_r = 2$, L_E, $E_c = 0.1$ and $\theta_w = 1$

K_r	N_T	N_B	M	$-\theta'(0)$	$-\phi'(0)$	$\phi(0)$
1	0.1	0.1	0.5	0.4664598246120293	0.26141498328150586	0.4771700334369882
2	0.1	0.1	0.5	0.5209896415637669	0.24716682675923912	0.5056663464815216
3	0.1	0.1	0.5	0.5442978732983028	0.23639158308557312	0.5272168338288539
4	0.1	0.1	0.5	0.5570914728351142	0.22923538494661175	0.5415292301067764
1	0.1	0.1	0.5	0.4664598246120293	0.26141498328150586	0.4771700334369882
1	0.3	0.1	0.5	0.37429846565406766	0.2595320125095193	0.48093597498096136
1	0.5	0.1	0.5	0.34622408550534034	0.2575302528333817	0.48493949433323646
1	0.7	0.1	0.5	0.33324873038809033	0.2554051792471895	0.48918964150562094
1	0.1	0.2	0.5	0.5231685965170045	0.2598771943047885	0.48024561139042277
1	0.1	0.3	0.5	0.5610775175261665	0.2565021697146164	0.48699566057076704
1	0.1	0.4	0.5	0.5754219014831572	0.25269787029430274	0.4946042594113944
1	0.1	0.8	0.5	0.5829394984132731	0.2484357738931433	0.5031284522137133
1	0.1	0.1	0	0.4708067434668121	0.2632332254073311	0.4735335491853378
1	0.1	0.1	1	0.4620367334127816	0.25957432652351636	0.4808513469529673
1	0.1	0.1	2	0.4529787582506981	0.2558032538839282	0.4883934922321435
1	0.1	0.1	3	0.4436266499078204	0.25163717722937007	0.49672564554125986

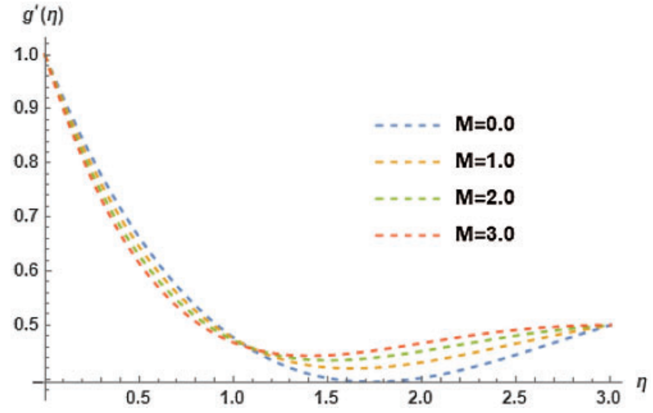

Figure 3: Velocity profile $g'(\eta)$ for different choices of M at $\gamma = 0.5$

The impact of radiation parameter K_r is depicted in Fig. 5. K_r impact on temperature profile $\phi(\eta)$ is studied in detail. It is observed that increase in Kr, first increases the temperature profile $\phi(\eta)$, followed by a decrease, and lastly, an increase is illustrated. Fig. 6 shows the Nusselt Number $\phi'(\eta)$ for diverse variations of radiation parameter K_r. It is observed that increase in K_r, first decreases the $\phi'(\eta)$, followed by an increase, and lastly, a decrease is noted. Illustration of the influence of Prandtl number P_R onto the dependent variable temperature profile $\phi(\eta)$ is presented in Fig. 7. Decreasing trend is observed in $\phi(\eta)$ with the increase in P_R. Effect of Prandtl Number P_R is studied on Nusselt number $\phi'(\eta)$ in Fig. 8. Increment in the P_R makes $\phi'(\eta)$ to increase and decrement of P_R causes $\phi'(\eta)$ to decrease. Hence, an increasing trend is comprehended by $\phi'(\eta)$.

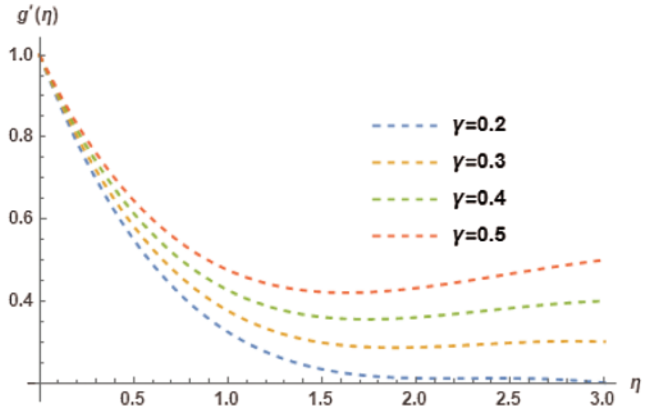

Figure 4: Velocity profile $g'(\eta)$ for different choices of γ at $M=1$

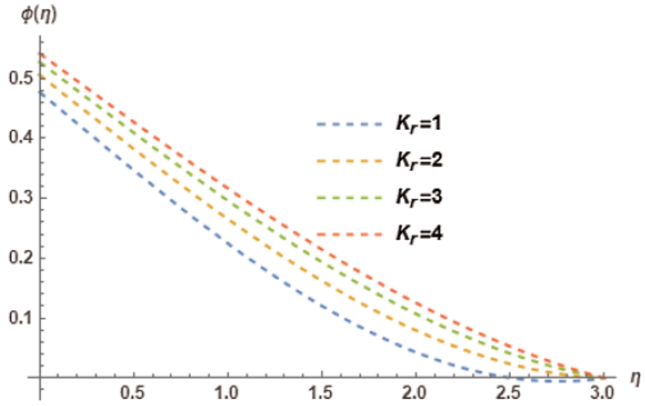

Figure 5: Temperature profile $\phi(\eta)$ for different choices of radiation parameter K_r at $M=1$, $\gamma=0.5$, $\lambda=0.4$, $P_R=3$, $N_B=0.1$, $N_T=0.1$, $L_E=2$, $E_c=0.2$, $\phi_w=1$ showing their exciting nature

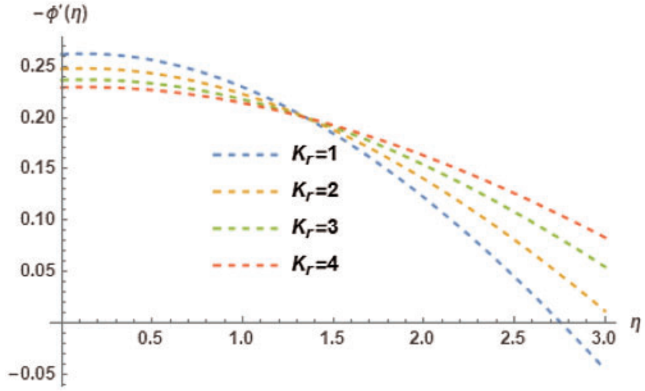

Figure 6: Nusselt number $-\phi'(\eta)$ for different choices of radiation parameter K_r at $M=1$, $\gamma=0.5$, $\lambda=0.4$, $P_R=3$, $N_B=0.1$, $N_T=0.1$, $L_E=2$, $E_c=0.2$, $\phi_w=1$ showing their exciting nature

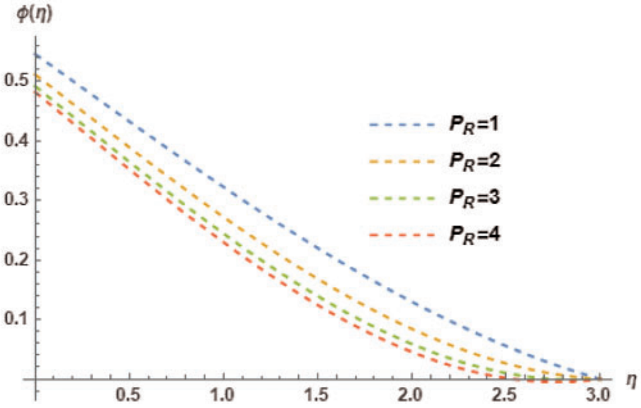

Figure 7: Temperature profile $\phi(\eta)$ for different choices of Prandtl number P_R at $M = 0.5$, $\gamma = 0.5$, $\lambda = 0.5$, $K_r = 2$, $N_B = 0.1$, $N_T = 0.1$, $L_E = 1$, $E_c = 0.2$, $\phi_w = 1$ showing their exciting nature

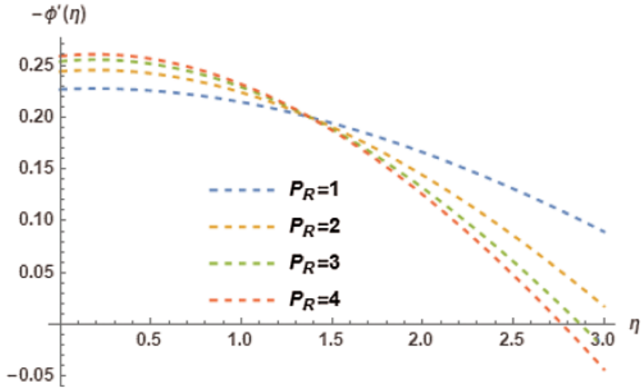

Figure 8: Nusselt number $-\phi'(\eta)$ for different choices of Prandtl number P_R at $M = 0.5$, $\gamma = 0.5$, $\lambda = 0.5$, $K_r = 2$, $N_B = 0.1$, $N_T = 0.1$, $L_E = 1$, $E_c = 0.2$, $\phi_w = 1$ showing their exciting nature

Influence on temperature profile $\phi(\eta)$ in accordance with Thermophoresis parameter N_T is discussed in Fig 9. The behavioral pattern comprehends it as an increasing trend. Fig. 10 shows the variation of N_T on the local nusselt number $\phi'(\eta)$. This figure elucidates $\phi'(\eta)$ with a decreasing trend in accordance with the variation of N_T. Brownian motion parameter N_B influences on temperature profile $\phi(\eta)$ is shown in Fig. 11. The Brownian motion in nanofluids exists due to their size and because of this size the effect of its minisicule particles play an important role in transfer of heat. The basis of definition of Brownian motion; hint towards the kinetic energy of nanoparticles increasing the values of $\phi(\eta)$ due to the chaotic motion intensity. Hence, an increasing trend is comprehended in $\phi(\eta)$. Brownian motion parameter N_B and its association with local Nusselt number is illustrated in Fig. 12. A decreasing trend has been comprehended by $\phi'(\eta)$ with the increase of N_T.

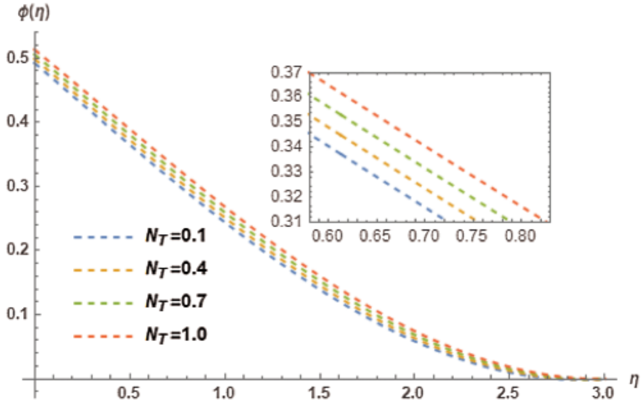

Figure 9: Influence of N_T on $\phi(\eta)$ at $M = 0.5$, $\gamma = 0.5$, $\lambda = 0.5$, $P_R = 4$, $K_r = 2$, $N_B = 0.1$, $L_E = 1$, $E_c = 0.2$, $\phi_w = 1$

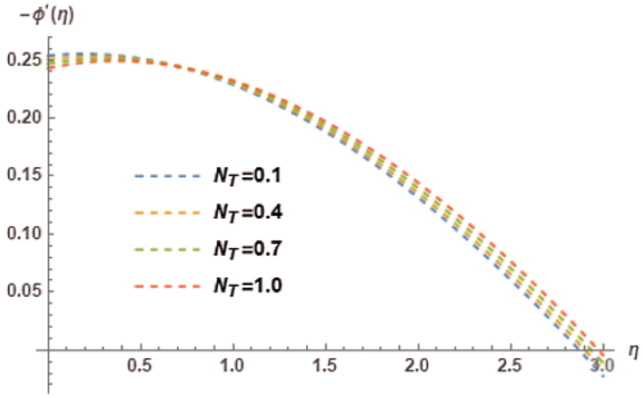

Figure 10: Variation of N_T on $-\phi'(\eta)$ at $M = 0.5$, $\gamma = 0.5$, $\lambda = 0.5$, $P_R = 4$, $K_r = 2$, $N_B = 0.1$, $L_E = 1$, $E_c = 0.2$, $\phi_w = 1$

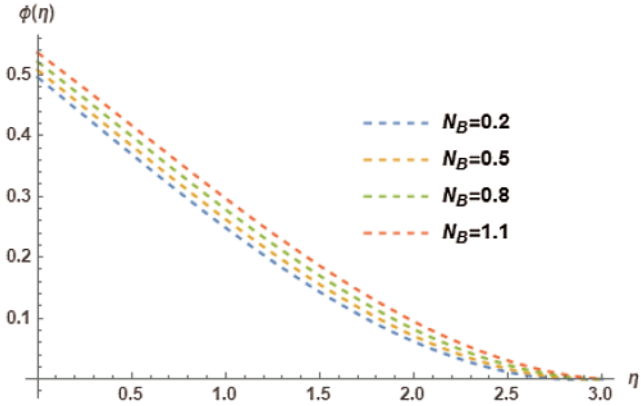

Figure 11: Influence of N_B on $\phi(\eta)$ at $M = 0.5$, $\gamma = 0.5$, $\lambda = 0.5$, $P_R = 4$, $K_r = 2$, $N_T = 0.1$, $L_E = 1$, $E_c = 0.2$, $\phi_w = 1$

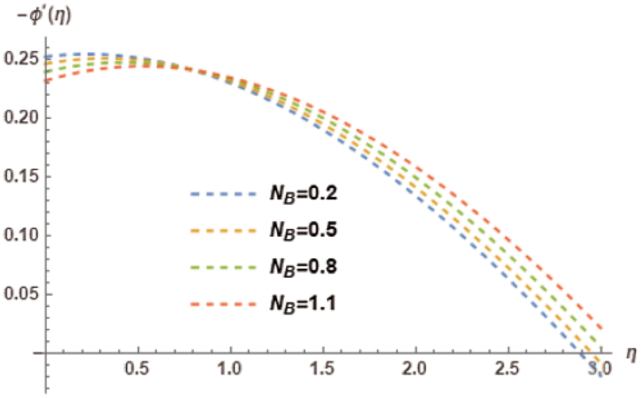

Figure 12: Variation of N_B on $-\phi'(\eta)$ at $M = 0.5$, $\gamma = 0.5$, $\lambda = 0.5$, $P_R = 4$, $K_r = 2$, $N_T = 0.1$, $L_E = 1$, $E_c = 0.2$, $\phi_w = 1$

Magnetic parameter's M effect on the temperature profile $\phi(\eta)$ is directed in Fig. 13. It is clearly noted that an increasing trend is comprehended by the $\phi(\eta)$ with the increment of M. Local Nusselt number $\phi'(\eta)$ and its resultant behavior associated with the effect of magnetic parameter M is depicted in Fig. 14. Magnetic parameter M causes a decreasing trend in $\phi'(\eta)$. Temperature profile $\phi(\eta)$ association with different values of of Lewis number L_E are depicted in Fig. 15. The behavioral pattern observed from the temperature profile $\phi(\eta)$ indicates it to be that of an increasing trend. Local Nusselts Number $\phi'(\eta)$ association with the diverse values of Lewis number L_E are represented in Fig. 16. The effect of L_E triggers the decreasing trend in $\phi'(\eta)$ is depicted.

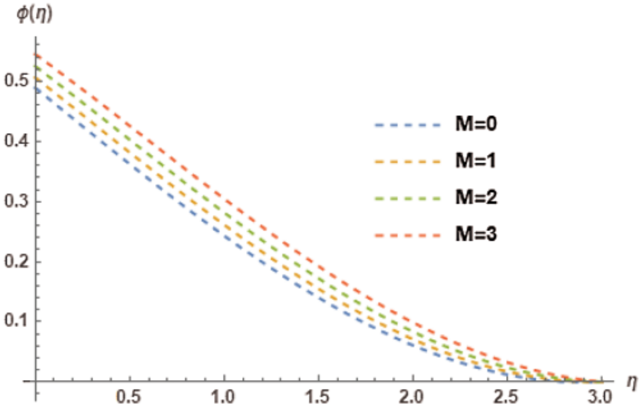

Figure 13: Temperature profile $\phi(\eta)$ for different choices of magnetic parameter M at $K_r = 3$, $\gamma = 0.5$, $\lambda = 0.4$, $P_R = 3$, $N_B = 0.1$, $N_T = 0.1$, $L_E = 2$, $E_c = 0.2$, $\phi_w = 1$ showing their exciting nature

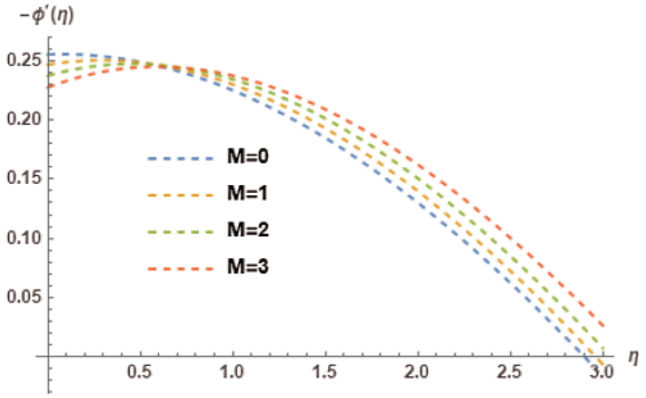

Figure 14: Nusselt number $-\phi'(\eta)$ for different choices of magnetic parameter M at $K_r = 3$, $\gamma = 0.5$, $\lambda = 0.4$, $P_R = 3$, $N_B = 0.1$, $N_T = 0.1$, $L_E = 2$, $E_c = 0.2$, $\phi_w = 1$ showing their exciting nature

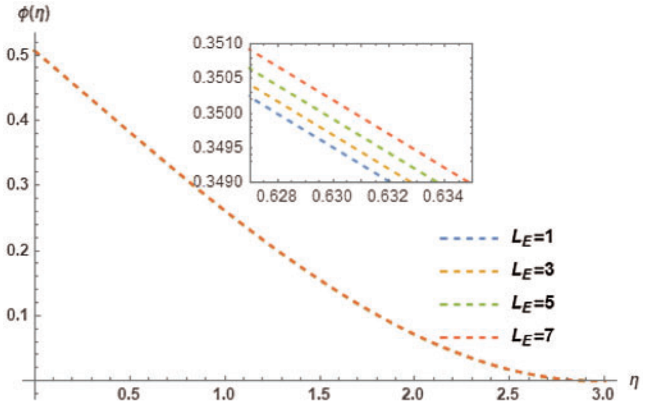

Figure 15: Temperature profile $\phi(\eta)$ for different choices of Lewis number L_E at $K_r = 3$, $\gamma = 0.5$, $\lambda = 0.4$, $P_R = 3$, $N_B = 0.1$, $N_T = 0.1$, $M = 1$, $E_c = 0.2$, $\phi_w = 1$ showing their exciting nature

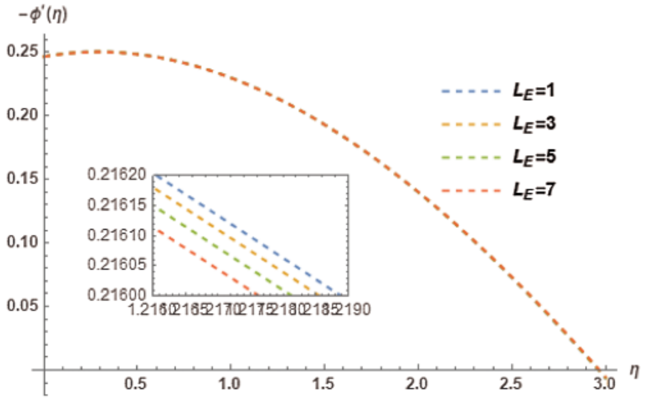

Figure 16: Nusselt number $-\phi'(\eta)$ for different choices of Lewis number L_E at $K_r = 3$, $\gamma = 0.5$, $\lambda = 0.4$, $P_R = 3$, $N_B = 0.1$, $N_T = 0.1$, $M = 1$, $E_c = 0.2$, $\phi_w = 1$ showing their exciting nature

Temperature profile and its association with different values of Eckert Number E_c are represented in Fig. 17. The different values of E_c invoke an increasing trend in the temperature profile $\phi(\eta)$. Fig. 18 showcases the effect of Eckert Number E_c on local Nusselt numbers $\phi'(\eta)$. The increase in E_c causes an inverse influence in $\phi'(\eta)$. This means that an increase in E_c will cause a decrease in $\phi'(\eta)$. Hence, a decreasing trend is comprehended in $\phi'(\eta)$. The impact of Biot number λ is reviewed in Fig. 19 in accordance with temperature profile $\phi(\eta)$. It is observed that increase in the λ will cause an increase in the $\phi(\eta)$. Hence an increasing trend has been comprehended in the temperature profile. Biot number λ and its impact on the local Nusselt number $\phi'(\eta)$ is demonstrated in Fig. 20. It is observed that λ will cause an increase in $\phi'(\eta)$. Therefore, an increasing trend is triggered in $\phi'(\eta)$.

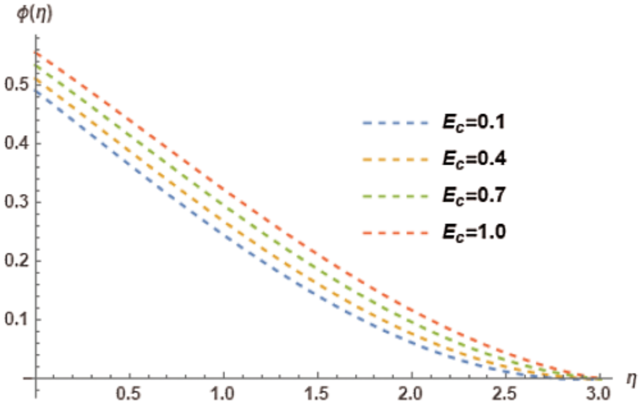

Figure 17: Influence of E_c on $\phi(\eta)$ at $M = 0.5$, $\gamma = 0.5$, $\lambda = 0.5$, $P_R = 4$, $K_r = 2$, $N_T = 0.1$, $L_E = 1$, $N_B = 0.1$, $\phi_w = 1$

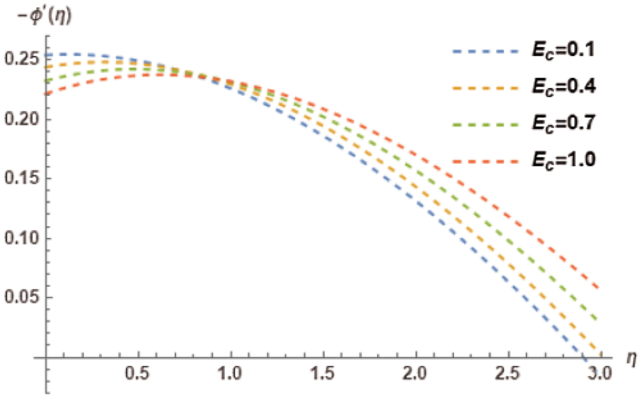

Figure 18: Variation of E_c on $-\phi'(\eta)$ at $M = 0.5$, $\gamma = 0.5$, $\lambda = 0.5$, $P_R = 4$, $K_r = 2$, $N_T = 0.1$, $L_E = 1$, $N_B = 0.1$, $\phi_w = 1$

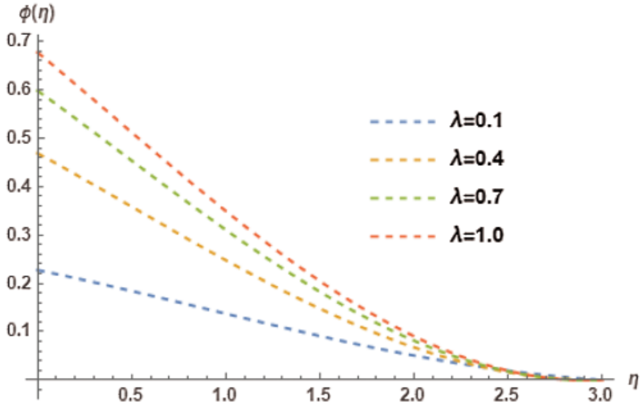

Figure 19: Influence of λ on $\phi(\eta)$ at $M = 0.5$, $\gamma = 0.5$, $E_c = 0.4$, $P_R = 4$, $K_r = 2$, $N_T = 0.1$, $L_E = 1$, $N_B = 0.1$, $\phi_w = 1$

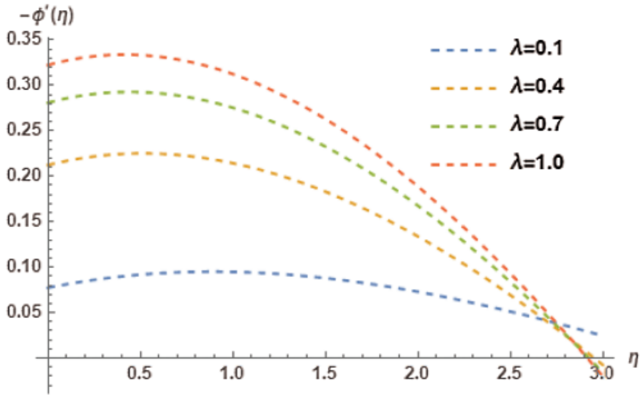

Figure 20: Variation of λ on $-\phi'(\eta)$ at $M = 0.5$, $\gamma = 0.5$, $E_c = 0.4$, $P_R = 4$, $K_r = 2$, $N_T = 0.1$, $L_E = 1$, $N_B = 0.1$, $\phi_w = 1$

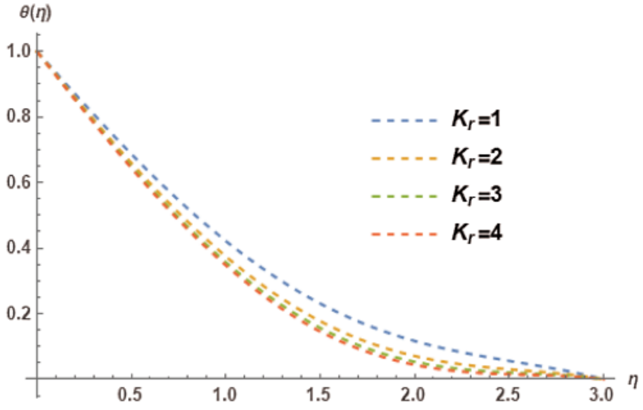

Figure 21: Nanoparticle concentration profile $\theta(\eta)$ for different choices of radiation parameter K_r at $M = 1$, $\gamma = 0.5$, $\lambda = 0.4$, $P_R = 3$, $N_B = 0.1$, $N_T = 0.1$, $L_E = 2$, $E_c = 0.2$, $\theta_w = 1$ showing their exciting nature

Fig. 21 represents the Nanoparticle concentration profile $\theta(\eta)$ and its association with diverse values of radiation parameter K_r. It is observed that the nanoparticles are elicited inversely with different variations of the radiation parameter. Thus a decreasing trend has been comprehended in $\theta(\eta)$. Different variations of radiation parameter K_r on Sherwood number $\theta'(\eta)$ is shown in Fig. 22. The increase in K_r also originates an increase in the $\theta'(\eta)$. Therefore an increasing trend is comprehended in $\theta'(\eta)$. Different values of Prandtl number P_R in association with Nanoparticle concentration profile $\theta(\eta)$ are presented in Fig. 23. The effect of different variations of P_R trigger an increasing trend in $\theta(\eta)$. Prandtl number P_R and its different values impact on the Sherwood number $\theta'(\eta)$ are revealed in Fig. 24. The different values of P_R inversely effect the $\theta'(\eta)$. Therefore a decreasing trend is observed in $\theta'(\eta)$.

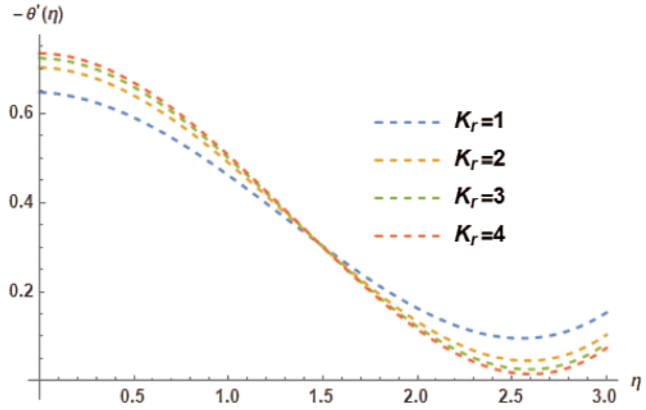

Figure 22: Sherwood number $-\theta'(\eta)$ for different choices of radiation parameter K_r at $M = 1$, $\gamma = 0.5$, $\lambda = 0.4$, $P_R = 3$, $N_B = 0.1$, $N_T = 0.1$, $L_E = 2$, $E_c = 0.2$, $\theta_w = 1$ showing their exciting nature

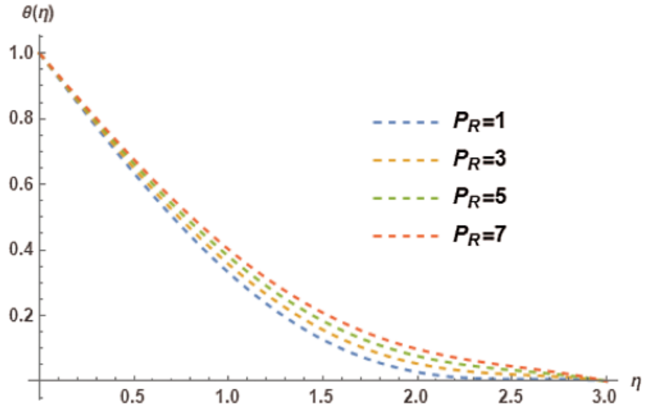

Figure 23: Nanoparticle concentration profile $\theta(\eta)$ for different choices of Prandtl number P_R at $M = 0.5$, $\gamma = 0.5$, $\lambda = 0.5$, $K_r = 2$, $N_B = 0.1$, $N_T = 0.1$, $L_E = 1$, $E_c = 0.2$, $\theta_w = 1$ showing their exciting nature

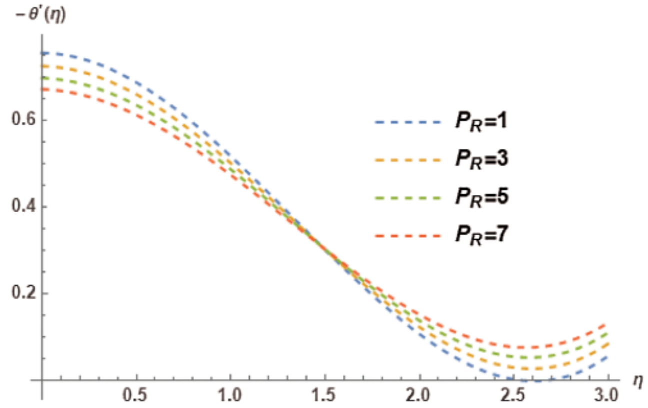

Figure 24: Sherwood number $-\theta'(\eta)$ for different choices of Prandtl number P_R at $M = 0.5$, $\gamma = 0.5$, $\lambda = 0.5$, $K_r = 2$, $N_B = 0.1$, $N_T = 0.1$, $L_E = 1$, $E_c = 0.2$, $\theta_w = 1$ showing their exciting nature

The thermophoresis parameter N_T and its association with Nanoparticle concentration profile $\theta(\eta)$ is represented in Fig. 25. The increase in N_T triggers an increasing trend in $\theta(\eta)$. Different values of thermophoresis parameter N_T and their impact on Sherwood number $\theta'(\eta)$ is revealed in Fig. 26. The different variations in N_T cause a decreasing trend in $\theta'(\eta)$. Brownian motion parameter N_B and its influence on Nanoparticle concentration profile $\theta(\eta)$ is discussed in Fig. 27. The different variations of N_B elicit a decreasing trend in $\theta(\eta)$. Brownian motion parameter N_B and its diverse values effect on the Sherwood number $\theta'(\eta)$ are presented in Fig. 28. It is observed that these variations elicit an increasing trend in $\theta'(\eta)$.

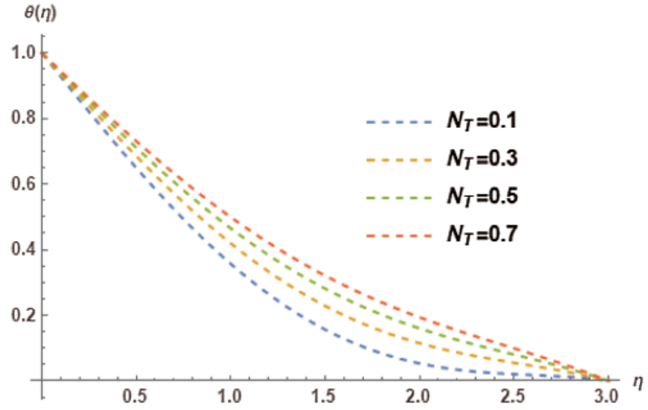

Figure 25: Influence of N_T on $\theta(\eta)$ at $M = 0.5$, $\gamma = 0.5$, $\lambda = 0.5$, $P_R = 4$, $K_r = 2$, $N_B = 0.1$, $L_E = 1$, $E_c = 0.2$, $\theta_w = 1$

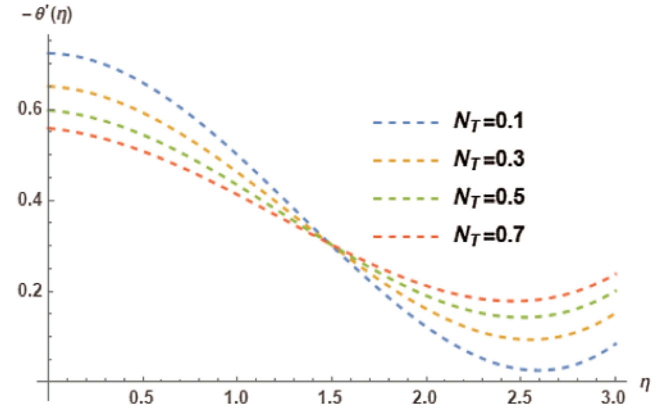

Figure 26: Variation of N_T on $-\theta'(\eta)$ at $M=0.5,\ \gamma=0.5,\ \lambda=0.5,\ P_R=4,\ K_r=2,\ N_B=0.1,\ L_E=1,\ E_c=0.2,\ \theta_w=1$

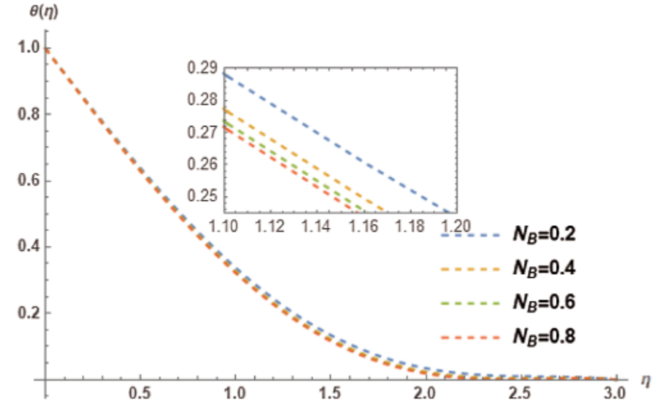

Figure 27: Influence of N_B on $\theta(\eta)$ at $M=0.5,\ \gamma=0.5,\ \lambda=0.5,\ P_R=4,\ K_r=2,\ N_T=0.1,\ L_E=1,\ E_c=0.2,\ \theta_w=1$

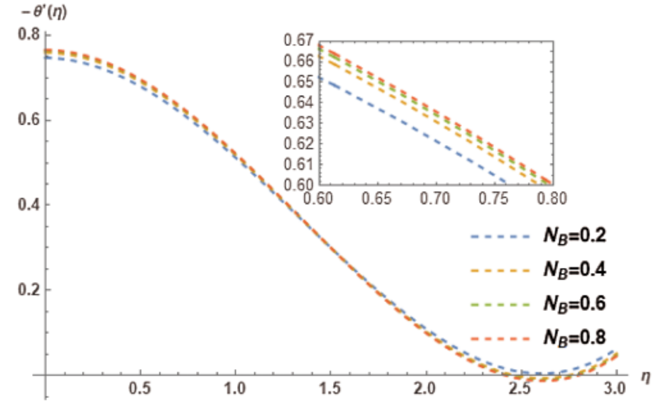

Figure 28: Variation of N_B on $-\theta'(\eta)$ at $M=0.5,\ \gamma=0.5,\ \lambda=0.5,\ P_R=4,\ K_r=2,\ N_T=0.1,\ L_E=1,\ E_c=0.2,\ \theta_w=1$

Diverse values of Lewis Number L_E and their impact on the Nanoparticle concentration profile $\theta(\eta)$ is illustrated in Fig. 29. The sudden increment in L_E resulted in somewhat greater difference because of it having weaker molecular diffusivity. This indicates that L_E triggers decreasing trend in $\theta(\eta)$. Lewis Number L_E and its different variations connotation with Sherwood number $\theta'(\eta)$ are illustrated in Fig. 30. The variations of L_E cause an increasing trend in $\theta'(\eta)$. The resultant values of Nanoparticle concentration profile $\theta(\eta)$ due to the impact of Eckert Number E_c are discussed in Fig. 31. This indicates a decreasing trend in $\theta(\eta)$. Eckert number E_c and its diverse value's association with the Sherwood number $\theta'(\eta)$ are illustrated in Fig. 32. The E_c effects the Sherwood number $\theta'(\eta)$ inversely. This indicates a decreasing trend in $\theta'(\eta)$. Biot number λ and its diverse values impact on Nanoparticle concentration profile $\theta(\eta)$ is presented in Fig. 33. It is observed that the Biot Number λ elicits an increasing trend in $\theta(\eta)$. Fig. 34 shows the variation of Biot number λ on the Sherwood number $\theta'(\eta)$. It is observed that the variations of λ inversely effect the $\theta'(\eta)$. This indicates a decreasing trend in $\theta'(\eta)$.

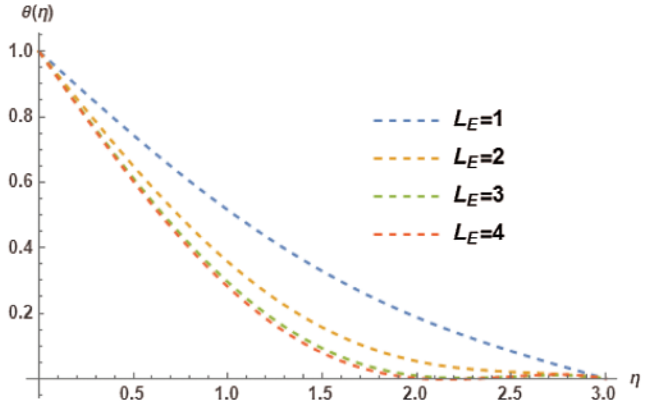

Figure 29: Nanoparticle concentration profile $\theta(\eta)$ for different choices of Lewis number L_E at $K_r = 3$, $\gamma = 0.5$, $\lambda = 0.4$, $P_R = 3$, $N_B = 0.1$, $N_T = 0.1$, $M = 1$, $E_c = 0.2$, $\theta_w = 1$ showing their exciting nature

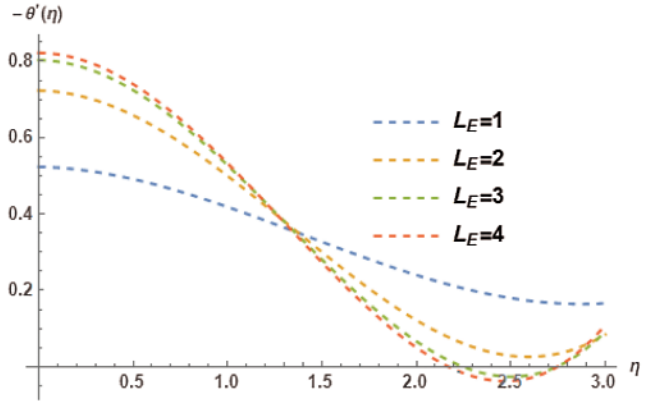

Figure 30: Sherwood number$-\theta'(\eta)$ for different choices of Lewis number L_E at $K_r = 3$, $\gamma = 0.5$, $\lambda = 0.4$, $P_R = 3$, $N_B = 0.1$, $N_T = 0.1$, $M = 1$, $E_c = 0.2$, $\theta_w = 1$ showing their exciting nature

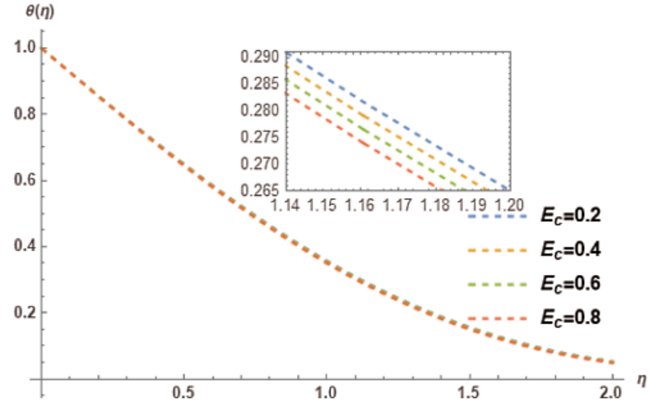

Figure 31: Influence of E_c on $\theta(\eta)$ at $M = 0.5$, $\gamma = 0.5$, $\lambda = 0.5$, $P_R = 4$, $K_r = 2$, $N_T = 0.1$, $L_E = 1$, $N_B = 0.1$, $\theta_w = 1$

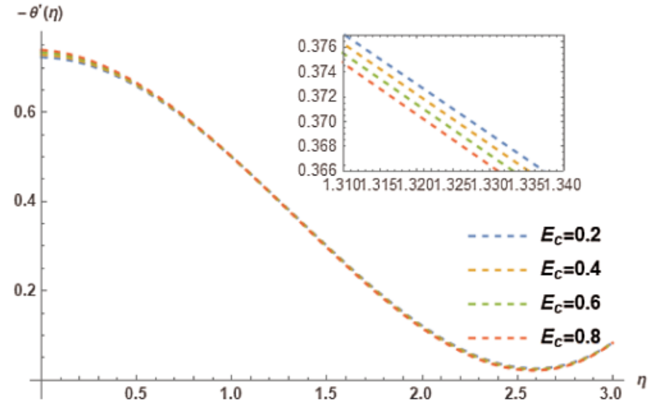

Figure 32: Variation of E_c on $-\theta'(\eta)$ at $M = 0.5$, $\gamma = 0.5$, $\lambda = 0.5$, $P_R = 4$, $K_r = 2$, $N_T = 0.1$, $L_E = 1$, $N_B = 0.1$, $\theta_w = 1$

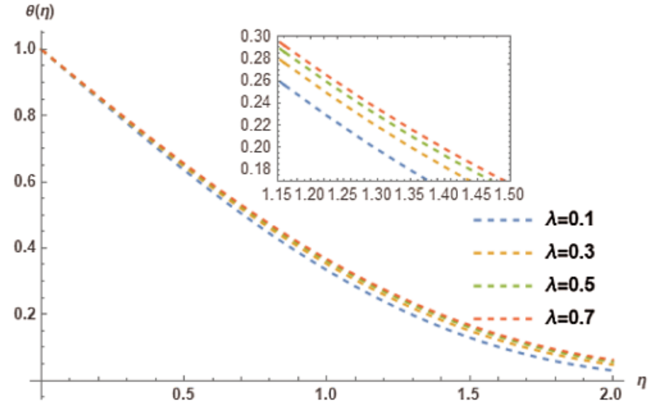

Figure 33: Influence of λ on $\theta(\eta)$ at $M = 0.5$, $\gamma = 0.5$, $E_c = 0.4$, $P_R = 4$, $K_r = 2$, $N_T = 0.1$, $L_E = 1$, $N_B = 0.1$, $\theta_w = 1$

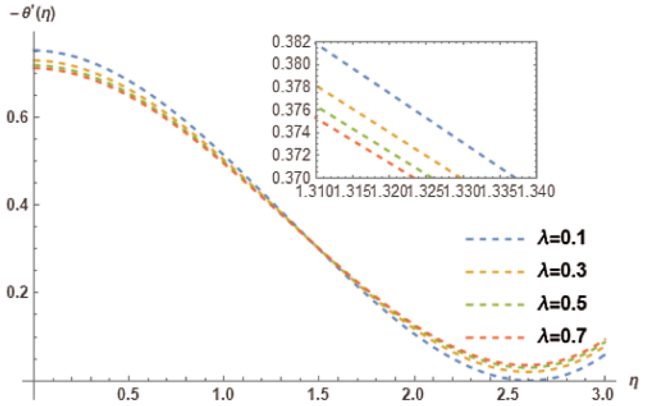

Figure 34: Variation of λ on $-\theta'(\eta)$ at $M = 0.5$, $\gamma = 0.5$, $E_c = 0.4$, $P_R = 4$, $K_r = 2$, $N_T = 0.1$, $L_E = 1$, $N_B = 0.1$, $\theta_w = 1$

5 Conclusion

This study exploits semi-analytical technique with changing aspects of the system. The system is based on a model with 2-D nanofluid flowing over a stretching sheet. This paper investigates the impact of Velocity profile $g(\eta)$, with the magnetic parameter M and $\gamma = \frac{\mu_\infty(x)}{\mu_w(x)}$. Influence on local Nusselt number $\phi'(\eta)$ and temperature profile $\phi(\eta)$ are also analyzed by varying magnetic field parameter M, radiation parameter K_r, Brownian motion parameter N_B, Prandtl number P_R, Biot number λ, Eckert number E_c, thermophoresis parameter N_T, and Sherwood number $\theta'(\eta)$. The Lewis number L_E and nanoparticle concentration Profile $\theta(\eta)$ are also analyzed graphically. The vital interpretations are as follows:

(1) It is observed velocity profile is decreasing with the Magnetic parameter M and increasing with the γ which is ratio between $\mu_\infty(x)$ and $\mu_w(x)$.

(2) Temperature profile $\phi(\eta)$ increases with Eckert number E_c, radiation parameter K_r, thermophoresis parameter N_T, magnetic parameter M, Brownian motion parameter N_B, Lewis number L_E, and Biot number λ. Temperature profile decreases $\phi(\eta)$ with Prandtl number P_R.

(3) The increase in local Nusselt number $\phi'(\eta)$ is invoked only with Biot number λ and Prandtl number P_R. The decrease in local Nusselt number $\phi'(\eta)$ is invoked with magnetic parameter M, radiation parameter K_r, Lewis number L_E, Brownian motion parameter N_B, thermophoresis parameter N_T, and Eckert number E_c.

(4) Nanoparticle concentration profile $\theta(\eta)$ increased with Biot number λ, thermophoresis parameter N_T and Prandtl number P_R. Decreasing trend for Nanoparticle concentration profile $\theta(\eta)$ was observed with Brownian motion parameter N_B, Lewis number L_E, and Eckert number E_c and radiation parameter K_r.

(5) Trend for Sherwood number $\theta'(\eta)$ was observed to increase with radiation parameter K_r, Lewis number L_E, and Brownian motion parameter N_B. Trend for Sherwood number $\theta'(\eta)$ was observed to decrease with Eckert number E_c, thermophoresis parameter N_T, Biot number λ and Prandtl number P_R.

Funding Statement: The authors received no specific funding for this study.

Conflicts of Interest: The authors declare that they have no conflicts of interest to report regarding the present study.

References

1. Hua, X., Zeng, Y., Wang, W., Shen, W. (2014). Light absorption mechanism of c-Si/a-Si half-coaxial nanowire arrays for nanostructured heterojunction photovoltaics. *IEEE Transactions on Electron Devices, 61(12),* 4007–4013. DOI 10.1109/TED.2014.2363001.
2. de Wild, J., Duindam, T., Rath, J., Meijerink, A., van Sark, W. et al. (2012). Increased upconversion response in a-Si: H solar cells with broad-band light. *IEEE Journal of Photovoltaics, 3(1),* 17–21. DOI 10.1109/JPHOTOV.2012.2213799.
3. Pakhuruddin, M. Z., Huang, J., Dore, J., Varlamov, S. (2015). Light absorption enhancement in laser-crystallized silicon thin films on textured glass. *IEEE Journal of Photovoltaics, 6(1),* 159–165. DOI 10.1109/JPHOTOV.5503869.
4. Chen, M., Zhang, Y., Cui, Y., Zhang, F., Qin, W. et al. (2017). Profiling light absorption enhancement in two-dimensional photonic-structured perovskite solar cells. *IEEE Journal of Photovoltaics, 7(5),* 1324–1328. DOI 10.1109/JPHOTOV.2017.2719759.
5. Ishizaki, K., Motohira, A., De Zoysa, M., Tanaka, Y., Umeda, T. et al. (2017). Microcrystalline-silicon solar cells with photonic crystals on the top surface. *IEEE Journal of Photovoltaics, 7(4),* 950–956. DOI 10.1109/JPHOTOV.2017.2695524.
6. Mehmood, U., Al-Ahmed, A., Afzaal, M., Hakeem, A. S., Haladu, S. A. et al. (2018). Enhancement of the photovoltaic performance of dye-sensitized solar cells by cosensitizing TiO_2 photoanode with uncapped pbs nanocrystals and ruthenizer. *IEEE Journal of Photovoltaics, 8(2),* 512–516. DOI 10.1109/JPHOTOV.5503869.
7. Liang, H., Liu, Y., Li, H., Zhang, H., Han, S. et al. (2018). All-fiber light intensity detector based on an ionic-liquid-adorned microstructured optical fiber. *IEEE Photonics Journal, 10(2),* 1–8. DOI 10.1109/JPHOT.4563994.
8. Ishii, S., Sugavaneshwar, R. P., Nagao, T. (2016). Titanium nitride nanoparticles as plasmonic solar heat transducers. *The Journal of Physical Chemistry C, 120(4),* 2343–2348. DOI 10.1021/acs.jpcc.5b09604.
9. Gondal, M., Rashid, S., Dastageer, M., Zubair, S., Ali, M. et al. (2013). Sol-gel synthesis of $Au/Cu-TiO_2$ nanocomposite and their morphological and optical properties. *IEEE Photonics Journal, 5(3),* 2201908–2201908. DOI 10.1109/JPHOT.2013.2262674.
10. Hogan, N. J., Urban, A. S., Ayala-Orozco, C., Pimpinelli, A., Nordlander, P. et al. (2014). Nanoparticles heat through light localization. *Nano Letters, 14(8),* 4640–4645. DOI 10.1021/nl5016975.
11. Ishii, S., Sugavaneshwar, R. P., Chen, K., Dao, T. D., Nagao, T. (2016). Solar water heating and vaporization with silicon nanoparticles at mie resonances. *Optical Materials Express, 6(2),* 640–648. DOI 10.1364/OME.6.000640.
12. Wang, Z., Tao, P., Liu, Y., Xu, H., Ye, Q. et al. (2014). Rapid charging of thermal energy storage materials through plasmonic heating. *Scientific Reports, 4(1),* 1–8. DOI 10.1038/srep06246.
13. Ghasemi, S. E., Hatami, M., Sarokolaie, A. K., Ganji, D. (2015). Study on blood flow containing nanoparticles through porous arteries in presence of magnetic field using analytical methods. *Physica E: Low-Dimensional Systems and Nanostructures, 70,* 146–156. DOI 10.1016/j.physe.2015.03.002.
14. Ghasemi, S. E., Hatami, M., Hatami, J., Sahebi, S., Ganji, D. (2016). An efficient approach to study the pulsatile blood flow in femoral and coronary arteries by differential quadrature method. *Physica A: Statistical Mechanics and its Applications, 443,* 406–414. DOI 10.1016/j.physa.2015.09.039.
15. Valipour, P., Ghasemi, S., Vatani, M. (2015). Theoretical investigation of micropolar fluid flow between two porous disks. *Journal of Central South University, 22(7),* 2825–2832. DOI 10.1007/s11771-015-2814-1.

16. Vatani, M., Ghasemi, S., Ganji, D. (2016). Investigation of micropolar fluid flow between a porous disk and a nonporous disk using efficient computational technique. *Proceedings of the Institution of Mechanical Engineers, Part E: Journal of Process Mechanical Engineering, 230(6),* 413–424. DOI 10.1177/0954408914557375.
17. Ghasemi, S., Hatami, M., Ganji, D. (2013). Analytical thermal analysis of air-heating solar collectors. *Journal of Mechanical Science and Technology, 27(11),* 3525–3530. DOI 10.1007/s12206-013-0878-0.
18. Ghasemi, S. E. (2017). Thermophoresis and brownian motion effects on peristaltic nanofluid flow for drug delivery applications. *Journal of Molecular Liquids, 238,* 115–121. DOI 10.1016/j.molliq.2017.04.067.
19. Ibrahim, W., Shankar, B., Nandeppanavar, M. M. (2013). Mhd stagnation point flow and heat transfer due to nanofluid towards a stretching sheet. *International Journal of Heat and Mass Transfer, 56(1),* 1–9. DOI 10.1016/j.ijheatmasstransfer.2012.08.034.
20. Mushtaq, A., Mustafa, M., Hayat, T., Alsaedi, A. (2014). Nonlinear radiative heat transfer in the flow of nanofluid due to solar energy: A numerical study. *Journal of the Taiwan Institute of Chemical Engineers, 45(4),* 1176–1183. DOI 10.1016/j.jtice.2013.11.008.
21. Ghasemi, S. E., Hatami, M., Jing, D., Ganji, D. (2016). Nanoparticles effects on mhd fluid flow over a stretching sheet with solar radiation: A numerical study. *Journal of Molecular Liquids, 219,* 890–896. DOI 10.1016/j.molliq.2016.03.065.
22. Mushtaq, A., Mustafa, M., Hayat, T., Alsaedi, A. (2014). Nonlinear radiative heat transfer in the flow of nanofluid due to solar energy: A numerical study. *Journal of the Taiwan Institute of Chemical Engineers, 45(4),* 1176–1183. DOI 10.1016/j.jtice.2013.11.008.
23. Awan, S. E., Raja, M. A. Z., Mehmood, A., Niazi, S. A., Siddiqa, S. (2020). Numerical treatments to analyze the nonlinear radiative heat transfer in mhd nanofluid flow with solar energy. *Arabian Journal for Science and Engineering, 45,* 4975–4994. DOI 10.1007/s13369-020-04593-5.
24. Marinca, V., Herisanu, N. (2015). Optimal homotopy asymptotic method. In: *The optimal homotopy asymptotic method,* pp. 9–22. Germany: Springer.
25. Marinca, V., Herisanu, N. (2008). Application of optimal homotopy asymptotic method for solving nonlinear equations arising in heat transfer. *International Communications in Heat and Mass Transfer, 35(6),* 710–715. DOI 10.1016/j.icheatmasstransfer.2008.02.010.
26. Herisanu, N. (2020). Optimal homotopy asymptotic approaches to nonlinear dynamical systems in engineering-4. *AIP Conference Proceedings,* vol. 2293. AIP Publishing LLC.
27. Marinca, V., Herisanu, N. (2010). Optimal homotopy perturbation method for strongly nonlinear differential equations. *Nonlinear Science Letters A, 1(3),* 273–280.
28. Iqbal, S., Javed, A. (2011). Application of optimal homotopy asymptotic method for the analytic solution of singular lane-emden type equation. *Applied Mathematics and Computation, 217(19),* 7753–7761. DOI 10.1016/j.amc.2011.02.083.
29. Manzoor, T., Nazar, K., Iqbal, S., Manzoor, H. U. (2021). Theoretical investigation of unsteady mhd flow within non-stationary porous plates. *Heliyon, 7(3),* e06567. DOI 10.1016/j.heliyon.2021.e06567.
30. Lane, H. J. (1870). On the theoretical temperature of the sun, under the hypothesis of a gaseous mass maintaining its volume by its internal heat, and depending on the laws of gases as known to terrestrial experiment. *American Journal of Science, 2(148),* 57–74. DOI 10.2475/ajs.s2-50.148.57.
31. Wazwaz, A. M. (2001). A new algorithm for solving differential equations of lane-emden type. *Applied Mathematics and Computation, 118(2),* 287–310. DOI 10.1016/S0096-3003(99)00223-4.